

Bending and Torsional Reconfiguration of Chiral Rods Under Wind and Gravity

Masoud Hassani^{a,*}, Simon Molgat Laurin^a, Njuki W. Mureithi^a, Frédéric P. Gosselin^{a,*}

^a*Department of Mechanical Engineering, École Polytechnique de Montréal
C.P. 6079, Succ. Centre-ville, Montréal, Québec, Canada H3C 3A7*

Abstract

We seek to understand the effect of chirality on the reconfiguration and the self-buckling strength of chiral plants subjected to wind and gravity by experimental and theoretical modeling of their large deformation. Chiral rod and ribbon specimens are made of polyurethane foam reinforced with nylon fibers and ABS plastic. Wind tunnel tests are performed to evaluate the effect of chirality on flow-induced reconfiguration. A theoretical model is developed by coupling the Kirchhoff rod theory with a semi-empirical formulation for aerodynamic loading evaluation. A range of geometrical, material and flow parameters are studied in the experimental and theoretical model. It is shown that for rods, chirality decreases the maximum root bending moment. For ribbons, chirality leads to a trade-off with higher self-buckling strength but also higher root bending moment. Moreover, chirality reduces the effect of the loading direction on deformation. Chirality plays an important structural role in the interaction of slender structures with fluid flow and gravity loading.

Key words: Reconfiguration, Drag reduction, Torsion, Large deformation, Buckling, Root bending moment, Kirchhoff rod.

1. Introduction

In general, plants and vegetation are flexible and are prone to significant deformation under fluid loading, their own weight or precipitation load. The deformation of plants which usually leads to a drag reduction, is termed reconfiguration [1]. The reconfiguration of plants has been studied fundamentally by modeling them as simple mechanical structures such as bending beams [2], fibers [3, 4] and plates [5, 6, 7]. Although these aforementioned models can simplify the two-dimensional deformation of plants, they are not representative for all forms of reconfiguration. For

*Corresponding author

Email addresses: frederick.gosselin@polymtl.ca (Frédéric P. Gosselin)

instance, many plants grow with a chiral morphology which cannot be modeled by a simple bending beam.

Chirality can be found in many biological and artificial structures, from DNA and several types of plants [8] to some polymers [9] and nano-materials [10, 11]. Many aquatic plants such as cattail, threeleaf arrowhead, sweet flag, bur-reed [8] and terrestrial plants such as daffodil and pancratium possess chiral leaves or stems [12]. In general, the evolutionary aspect of chirality in biological structures has been discussed in many studies. For instance, it is of great interest to know whether the chiral morphology of DNA was a requirement or an outcome of evolution [13]. Moreover, it has been claimed in some studies that erect plants with chiral morphology are less vulnerable to distributed transverse loading and Euler buckling [8, 12, 14]. The latter may be evidence of adaptation of this type of plants to their environment through a long evolution process.

Chiral structures have been studied mathematically using different theories such as Timoshenko pre-twisted beams [8, 12], Kirchhoff rods [11, 15, 16], and Cosserat rods [17]. However, the mathematical study of the large deformation of chiral plants bending and twisting in flow is missing from the literature. Therefore, the goal of this work is to study the reconfiguration mechanisms of chiral plants subjected to wind and gravity through a combination of chiral rod simulations and wind tunnel experiments. We seek to understand the effect of chirality on the ability of plants to withstand the fluid loading and their own weight.

2. Methodology

2.1. Experimental Procedure and Materials

The tests on flexible specimens with chiral morphology were performed in a wind tunnel located at École Nationale d'Aérotechnique (Saint-Hubert, QC, Canada). The wind tunnel has a square test section of $60 \times 60 \text{ cm}^2$ and can produce a maximum air speed of 38 ms^{-1} . As detailed in Ref. [18], a six-axis force transducer (ATI GAMMA, ATI Industrial Automation, Apex, North Carolina) was used in the present experiments to measure the aerodynamic forces and moments in three orthogonal directions. It can measure transverse forces, axial forces and moments up to 32 N, 100 N and 2.5 Nm, respectively. The resolution of the force transducer is $6.25 \times 10^{-3} \text{ N}$ and $12.5 \times 10^{-3} \text{ N}$ for the transverse and axial loading and $0.5 \times 10^{-3} \text{ Nm}$ for moments. The force transducer was fixed to the top of the wind tunnel test section. The specimens were clamped to the force balance at one end using a mast to subtract the effect of boundary layer on the tunnel wall from the measurements. In each test, the

root incidence angle of a specimen was fixed within a range of $\psi_0 = 0^\circ$ to 90° or 90° to 180° , then the flow velocity was increased from 3.5 ms^{-1} to more than 30 ms^{-1} depending on the stability of the specimen. A Labview code was used to acquire and save aerodynamic forces and moments.

Two types of flexible specimens were used in the experiments: circular rods and flat ribbons. The circular rods are made using polyurethane foam and are internally reinforced with nylon fibers as described in [18] and the supplementary file. The fibers are positioned along one diameter of a cylindrical mold and twisted around its centerline. Foam is poured and left to expand in the closed mold, then cure over several hours. As a result, the rod is conferred with anisotropic bending rigidity $(EI)_y/(EI)_x < 1$ and a natural twist (Fig 1a). To evaluate the uniformity of foam rods, a specimen was cut to smaller pieces of equal size. Measuring the weight of pieces showed that the density of the foam varies by approximately seven percent along the length of a rod, which is uniform enough for the purpose of this study. Moreover, the foam rigidity is significantly smaller than that of fibers therefore the effect of this non-uniformity is minimized. To maintain the uniformity of fibers inside the foam, they were kept apart with small spacers to ensure a uniform twist and a constant distance between them. A circular section was used in order to simplify the fluid loading evaluation in the theoretical model. The flat ribbons, on the other hand, have intrinsic directional rigidity due to their greater-than-unity width to thickness ratio (Fig 1b). They are made of ABS plastic and twisted along their length with a range of intrinsic twist angles τ_0 . Annealing at 100 C for several hours was performed to make the twisted state of the rods their stress-free state (see the supplementary file for more detail).

The anisotropic bending rigidity of the rods and the ribbons form a material frame $(\mathbf{e}_x, \mathbf{e}_y, \mathbf{e}_z)$ where \mathbf{e}_y is along the more rigid direction (Fig 1c and d) and \mathbf{e}_z is tangent to the centerline (Fig 1e). For a chiral ribbon, fluid loading depends on the alignment of its sections with respect to the flow direction i.e. the local angle of incidence ψ [18]. The directional rigidity gives rise to a three-dimensional deformation in asymmetric bending. In the tests, the clamped end of each specimen was rotated around its centerline to have different values of incidence angle at the clamped end ψ_0 . Eleven specimens, as listed in Table 1, were made for a range of intrinsic twist angles τ_0 varying from 0° to 720° . The specimens named C are circular reinforced rods made of polyurethane foam and the specimens named S are ribbons made of ABS plastic. Three-points bending tests were performed with a universal testing frame to evaluate the bending rigidity of the rods and ribbons. The Young's modulus for all ribbon specimens is the same. For the circular rods, it is assumed that the Young's

modulus of the foam part has a linear relation with the rod's density. The maximum and minimum bending rigidity for a circular rod with $\tau_0 = 0^\circ$ was measured and the rigidity of the other circular rods was reconstructed based on the aforementioned assumption.

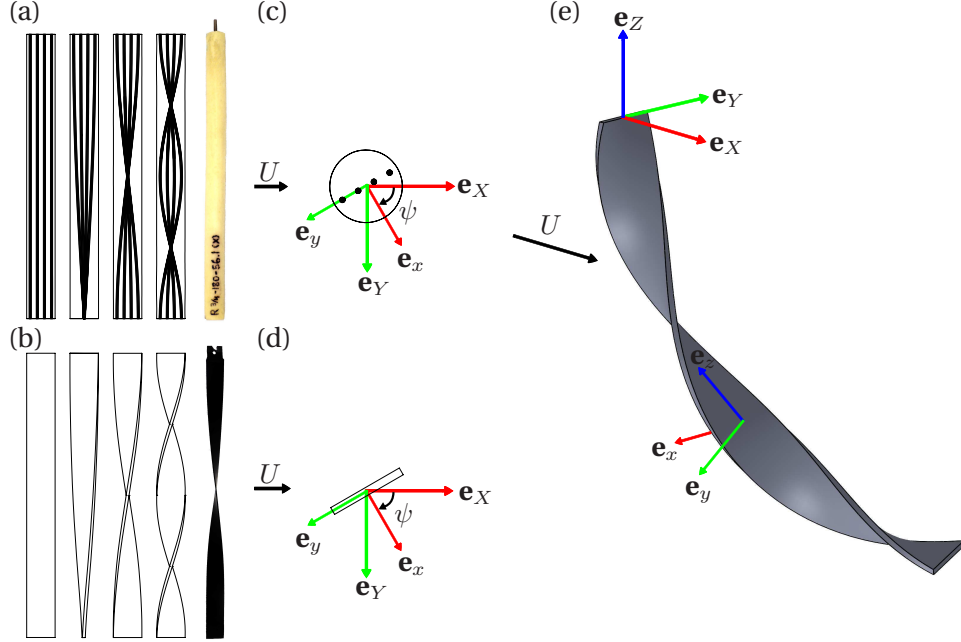


Figure 1: a) Schematics of chiral rods with an intrinsic twist angle varying from 0° to 360° as well as a real rod specimen. b) Schematics of chiral ribbons with an intrinsic twist angle varying from 0° to 360° as well as a real twisted ribbon. c) Section of a chiral rod and d) section of a chiral ribbon both with an incidence angle of ψ . e) Schematic of a chiral ribbon deformed in the flow with a moving material frame attached to its centerline.

2.2. Theoretical Model

The three-dimensional reconfiguration of chiral structures is modeled theoretically using the Kirchhoff theory of rods. In the model, a rod is represented by a deforming three-dimensional and inextensible curve with the assumption of small strains [19]. It is also assumed that each cross section of the rod remains planar and normal to the centerline. The rod is attached to a fixed coordinate system $(\mathbf{e}_X, \mathbf{e}_Y, \mathbf{e}_Z)$ from one end and moving material frames $(\mathbf{e}_x, \mathbf{e}_y, \mathbf{e}_z)$ are attached to its centerline (Fig 1e). Bending moments and the twisting moments are proportional to the curvatures, (κ_x, κ_y) and the twist (τ) , respectively:

$$M_x = (EI)_x \kappa_x, \quad M_y = (EI)_y \kappa_y, \quad M_z = GJ\tau, \quad (1)$$

where $(EI)_y$ and $(EI)_x$ are the bending rigidities and GJ is the torsional rigidity. In this model, the natural twist and curvature of a rod is represented by $\kappa_{x,0}$, $\kappa_{y,0}$ and τ_0 . As detailed in Ref. [18], the equilibrium Kirchhoff equations are:

$$\frac{dN_x}{ds} = N_y\tau - T\kappa_y - P_x - W_x, \quad (2)$$

$$\frac{dN_y}{ds} = T\kappa_x - N_x\tau - P_y - W_y, \quad (3)$$

$$\frac{dT}{ds} = N_x\kappa_y - N_y\kappa_x - P_z - W_z, \quad (4)$$

$$(EI)_x \frac{d\kappa_x}{ds} = (EI)_y(\kappa_y - \kappa_{y,0})\tau - GJ(\tau - \tau_0)\kappa_y + N_y, \quad (5)$$

$$(EI)_y \frac{d\kappa_y}{ds} = GJ(\tau - \tau_0)\kappa_x - (EI)_x(\kappa_x - \kappa_{x,0})\tau - N_x, \quad (6)$$

$$GJ \frac{d\tau}{ds} = (EI)_x(\kappa_x - \kappa_{x,0})\kappa_y - (EI)_y(\kappa_y - \kappa_{y,0})\kappa_x, \quad (7)$$

where N_x and N_y are shear forces and T is the internal tensile force. Moreover, P is the external loading and $W = mgL^{-1}$ is the weight per unit length in the Z -direction, both decomposed in the three directions of the material frame. The material frame $(\mathbf{e}_x, \mathbf{e}_y, \mathbf{e}_z)$ is related to the fixed frame $(\mathbf{e}_X, \mathbf{e}_Y, \mathbf{e}_Z)$ through the direction cosine matrix $[c]$:

$$\begin{Bmatrix} \mathbf{e}_x \\ \mathbf{e}_y \\ \mathbf{e}_z \end{Bmatrix} = \begin{bmatrix} c_{11} & c_{12} & c_{13} \\ c_{21} & c_{22} & c_{23} \\ c_{31} & c_{32} & c_{33} \end{bmatrix} \begin{Bmatrix} \mathbf{e}_X \\ \mathbf{e}_Y \\ \mathbf{e}_Z \end{Bmatrix}. \quad (8)$$

The direction cosines represent the rotation of the material frame and they are the cosines of the angles between a direction of the material frame and the directions of the fixed frame. The spatial

Table 1: Physical properties of tested specimens

Specimen	L (cm)	d (cm)	t (cm)	$(EI)_y$ (Nm ²)	$\frac{(EI)_y}{GJ}$	$\frac{(EI)_y}{(EI)_x}$	Weight (g)	Twist τ_0
C1	26	1.9	-	0.0036	1.25	0.16	25	0°
C2	26	1.9	-	0.0036	1.25	0.16	25	90°
C3	26	1.9	-	0.0036	1.25	0.16	25	180°
C4	26	1.9	-	0.0029	1.25	0.13	20	270°
C5	26	1.9	-	0.0029	1.25	0.13	20	360°
C6	26	1.9	-	0.0029	1.25	0.13	20	720°
S1	40	2.5	0.12	0.010	0.675	0.0022	13	0°
S2	40	2.5	0.12	0.010	0.675	0.0022	13	90°
S3	40	2.5	0.12	0.010	0.675	0.0022	13	180°
S4	40	2.5	0.12	0.010	0.675	0.0022	13	270°
S5	40	2.5	0.12	0.010	0.675	0.0022	13	360°

derivative of a direction of the material frame with respect to the arclength s is [20]:

$$\frac{d\mathbf{e}_i}{ds} = \boldsymbol{\Omega} \times \mathbf{e}_i, \quad (9)$$

where \mathbf{e}_i is a direction of the material frame and $\boldsymbol{\Omega}$ is the *Darboux vector*:

$$\boldsymbol{\Omega} = \kappa_x \mathbf{e}_x + \kappa_y \mathbf{e}_y + \tau \mathbf{e}_z. \quad (10)$$

Substituting Eq.(10) in Eq.(9) leads to a system of nine equations, six of which are independent. In the model, the six independent spatial derivative equations are coupled with the Kirchhoff equations (Eq.(2) to Eq.(7)) to define the full state of the deformed rod.

A semi-empirical formulation of the aerodynamic force on a rod is also used to evaluate the loading on the deformed specimens [18, 21]. In this method, the local lift and drag of a rod element depends only on the element's orientation and the normal component of the flow velocity to the centerline at the element. The flow velocity is taken to be in the X -direction:

$$\mathbf{U} = U \mathbf{e}_X = U_z \mathbf{e}_z + U_n \mathbf{e}_n, \quad (11)$$

where U is the magnitude of the flow velocity and \mathbf{e}_n is the direction normal to the centerline in the XZ -plane. The local angle α between the centerline of the rod and the flow velocity direction is:

$$\cos \alpha = \mathbf{e}_z \cdot \mathbf{e}_X = c_{31}, \quad \sin \alpha = \sqrt{1 - c_{31}^2}. \quad (12)$$

Therefore, the component of flow velocity normal to the centerline is:

$$U_n = U \sqrt{1 - c_{31}^2}. \quad (13)$$

The friction drag along the centerline produced by $U_z \mathbf{e}_z$ is not considerable therefore we neglect it in the model. The drag normal to the centerline per unit length is in the direction of the normal velocity:

$$\mathbf{D} = \frac{1}{2} \rho d C_D U_n^2 \mathbf{e}_n, \quad (14)$$

where C_D is the drag coefficient. Similarly, the normal lift force per unit of length is written as:

$$\mathbf{L} = \frac{1}{2} \rho d C_L U_n^2 \mathbf{e}_l, \quad (15)$$

where C_L is the lift coefficient and \mathbf{e}_l is the direction of the normal lift force. The direction of the normal drag \mathbf{e}_n is parallel to the projection of \mathbf{e}_X on the xy -plane:

$$\mathbf{e}_n = \frac{\mathbf{e}_X - (\mathbf{e}_X \cdot \mathbf{e}_z) \mathbf{e}_z}{|\mathbf{e}_X - (\mathbf{e}_X \cdot \mathbf{e}_z) \mathbf{e}_z|} = \frac{c_{11} \mathbf{e}_x + c_{21} \mathbf{e}_y}{\sqrt{1 - c_{31}^2}}, \quad (16)$$

Similarly, the direction of the normal lift \mathbf{e}_l is parallel to the projection of \mathbf{e}_Y on the xy -plane:

$$\mathbf{e}_l = \frac{\mathbf{e}_Y - (\mathbf{e}_Y \cdot \mathbf{e}_z) \mathbf{e}_z}{|\mathbf{e}_Y - (\mathbf{e}_Y \cdot \mathbf{e}_z) \mathbf{e}_z|} = \frac{c_{12} \mathbf{e}_x + c_{22} \mathbf{e}_y}{\sqrt{1 - c_{32}^2}}. \quad (17)$$

By extending this approach, the normal lift and drag forces of a deformed ribbon element δs can be evaluated locally by introducing the sectional drag and lift coefficients $C_D(s)$ and $C_L(s)$ which depend on the local orientation of the rod. This is based on the assumption that the cross section of rods and ribbons does not deform. To evaluate the sectional drag and lift coefficients for ribbons whether chiral or straight, wind tunnel measurements are performed on rigid straight metallic strips with a similar geometry and the same sectional aspect ratio $\sqrt{(I_x/I_y)}$ for a range of angles of incidence ψ_0 . Consequently, the variation of C_D and C_L as a function of the angle of incidence is obtained for a rectangular section. In addition, the variation of the sectional angle of incidence for a deformed ribbon, as a function of the arc length s , is calculated in the mathematical model. Therefore, C_D and C_L as a function of the arc length s can be evaluated. For a circular rod, $C_D(s)$ is a constant and $C_L(s)$ is null. It is assumed that for Reynolds numbers within the range of 10^3 to 10^5 , the drag and lift coefficients do not change with flow velocity.

The external loading P in Eq.(2) to Eq.(4) for a rod in fluid flow is the resultant of the drag and lift forces. By decomposing the external loading in the directions of the material frame we have:

$$P_x = \mathbf{D} \cdot \mathbf{e}_x + \mathbf{L} \cdot \mathbf{e}_x, \quad (18)$$

$$P_y = \mathbf{D} \cdot \mathbf{e}_y + \mathbf{L} \cdot \mathbf{e}_y, \quad (19)$$

$$P_z = 0. \quad (20)$$

The angle between the x and y -components of the normal drag is the sectional angle of incidence. Therefore, using Eq.(18) and Eq.(19)

$$\psi = \arctan\left(-\frac{c_{21}}{c_{11}}\right). \quad (21)$$

In the model we assume that the positive rotation is clockwise thus a negative sign is imposed in Eq.(21).

2.2.1. Dimensionless Equations

Dimensionless Kirchhoff equations of a deforming rod are written using the Cauchy number:

$$C_Y = \frac{\rho U^2 L^3 d}{2(EI)_y}. \quad (22)$$

The Cauchy Number is the ratio of the fluid force to the minimum bending rigidity of the flexible body [6, 22, 23]. The following dimensionless parameters are also introduced in the Kirchhoff equations [18]:

$$\begin{aligned} \bar{s} &= s/L & \bar{\kappa}_x &= \kappa_x L & \bar{\kappa}_y &= \kappa_y L & \bar{\tau} &= \tau L, \\ \bar{N}_x &= \frac{N_x L^2}{(EI)_y} & \bar{N}_y &= \frac{N_y L^2}{(EI)_y} & \bar{T} &= \frac{TL^2}{(EI)_y} & \mathcal{W} &= \frac{mgL^2}{(EI)_y}. \end{aligned}$$

By introducing the aforementioned dimensionless parameters in Eq.(2) to Eq.(7), dimensionless Kirchhoff equations are written as follows:

$$\frac{d\bar{N}_x}{d\bar{s}} = \bar{N}_y \bar{\tau} - \bar{T} \bar{\kappa}_y - \bar{P}_x - \mathcal{W}_x, \quad (23)$$

$$\frac{d\bar{N}_y}{d\bar{s}} = \bar{T} \bar{\kappa}_x - \bar{N}_x \bar{\tau} - \bar{P}_y - \mathcal{W}_y, \quad (24)$$

$$\frac{d\bar{T}}{d\bar{s}} = \bar{N}_x \bar{\kappa}_y - \bar{N}_y \bar{\kappa}_x - \bar{P}_z - \mathcal{W}_z, \quad (25)$$

$$\frac{d\bar{\kappa}_x}{d\bar{s}} = \lambda(\bar{\kappa}_y - \bar{\kappa}_{y,0})\bar{\tau} - \left(\frac{\lambda}{\eta}\right)(\bar{\tau} - \bar{\tau}_0)\bar{\kappa}_y + \lambda\bar{N}_y, \quad (26)$$

$$\frac{d\bar{\kappa}_x}{d\bar{s}} = \left(\frac{1}{\eta}\right)(\bar{\tau} - \bar{\tau}_0)\bar{\kappa}_x - \left(\frac{1}{\lambda}\right)(\bar{\kappa}_x - \bar{\kappa}_{x,0})\bar{\tau} - \bar{N}_x, \quad (27)$$

$$\frac{d\bar{\tau}}{d\bar{s}} = \left(\frac{\eta}{\lambda}\right)(\bar{\kappa}_x - \bar{\kappa}_{x,0})\bar{\kappa}_y - \eta(\bar{\kappa}_y - \bar{\kappa}_{y,0})\bar{\kappa}_x, \quad (28)$$

where the dimensionless external forces are

$$\bar{P}_x = C_Y C_D(s) \sqrt{(1 - c_{31}^2)} c_{11} + C_Y C_L(s) \frac{1 - c_{31}^2}{1 - c_{32}^2} c_{12}, \quad (29)$$

$$\bar{P}_y = C_Y C_D(s) \sqrt{(1 - c_{31}^2)} c_{21} + C_Y C_L(s) \frac{1 - c_{31}^2}{1 - c_{32}^2} c_{22}. \quad (30)$$

Dimensionless parameters λ and η are the bending rigidity ratio and the twist-to-bend ratio, respectively [18]:

$$\lambda = \frac{(EI)_y}{(EI)_x}, \quad (31)$$

$$\eta = \frac{(EI)_y}{GJ}. \quad (32)$$

Since the dimensionless weight of the rod is in the Z -direction of the fixed frame, it is decomposed in the three directions of the material frame as:

$$\mathcal{W}_x = \mathcal{W}.c_{31}, \quad (33)$$

$$\mathcal{W}_y = \mathcal{W}.c_{32}, \quad (34)$$

$$\mathcal{W}_z = \mathcal{W}.c_{33}. \quad (35)$$

The system of equations including Eq.(23) to Eq.(28) coupled with Eq.(9) is solved using MATLAB as a boundary value problem using the `bvp4c` solver. As explained in [18], a continuation approach is used to solve the system of equations. In the method, an initial guess for all twelve variables is considered. The solution is then evaluated step by step for an increasing Cauchy number. This approach is continued up to a higher limit of Cauchy number i.e. 1000. However, to study the cases including a static instability such as buckling, the governing equations are solved using AUTO [24]. This software package solves problems which can include bifurcations. In the software, a continuation parameter is considered and the governing equations are solved for a range of that parameter. For this buckling problem, the dimensionless weight \mathcal{W} is the continuation parameter. A cross-comparison has been done for cases without bifurcation between the MATLAB code and the AUTO solver which show identical results to seven significant figures [18].

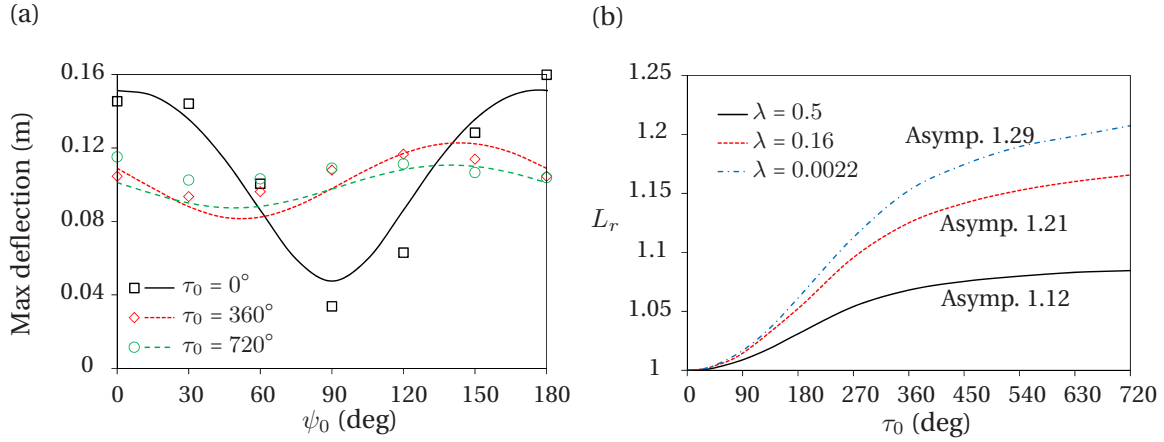


Figure 2: a) Static bending test for chiral circular rods. The rods are fixed horizontally from one end and their maximum vertical deflection is plotted vs. the angle of incidence at the fixed end. Markers represent the experimental results. b) The effect of chirality and the bending rigidity ratio of rods on their critical buckling length.

3. Results and Discussion

3.1. Mathematical Model Verification

A comparison has been performed in Ref. [18] on the three-dimensional deformed shape of non-chiral rods, obtained from wind tunnel tests and the present mathematical model. Herein, only the validation of the chirality component in the mathematical model is investigated. To validate the mathematical model, the numerical and experimental results for the deformation of circular chiral rods with different τ_0 are presented in Fig. 2a. In the test, the rods were clamped from one end horizontally, and deforming under their own weight. Each specimen was rotated around its centerline to have different values of incidence angle at the clamped end ψ_0 . In the figure, the tip vertical deflection is plotted as a function of the incidence angle for three different intrinsic twist angles. Markers represent the measured values and curves represent the mathematical prediction. Results show that the maximum vertical deflection and consequently the effective bending rigidity varies with the incidence angle ψ_0 . Moreover, by increasing the intrinsic twist angle, the deflection of the rods becomes less dependent upon the direction of loading. The mathematical model shows good agreement with the experimental results. Another verification is carried out by comparing the measured drag and lift coefficients of a rigid twisted rod ($\tau_0 = 90^\circ$) with the mathematical model which is provided in the supplementary file.

3.2. Buckling

It has been noted that chirality is beneficial to plants since it increases their strength against buckling under their own weight or that of their head organ [8, 12]. We study the buckling of chiral ribbons and rods under their own weight which are similar to upright slender plants without a head organ such as a cattail leaf. Figure 2b illustrates the effect of chirality on the relative critical length of buckling $L_r = L_{cr}/L_{cr,0}$ where $L_{cr,0}$ is the critical length of a non-chiral rod or ribbon ($\tau_0 = 0^\circ$) buckling in the plane of least resistance ($\psi_0 = 0^\circ$). It should be mentioned that according to our mathematical modeling and also the Euler buckling theory, $L_{cr,0} \approx \sqrt[3]{7.837(EI)_y/\gamma}$ for a self weight buckling case where γ is the weight per unit length. In the figure, L_r is plotted for several bending rigidity ratios and for a range of intrinsic twist angle from 0° to 720° . Each curve corresponds to a value of the bending rigidity ratio while the other structural parameters are kept constant. It is shown that increasing the intrinsic twist angle increases the critical buckling length meaning that the buckling strength is increased. Moreover, decreasing the bending rigidity ratio or equivalently increasing the sectional aspect ratio, increases the influence of chirality on the critical buckling length. This means that chirality is more effective for ribbons with a small λ than rods with a circular section and large λ . In addition, the twist-to-bend ratio η does not affect the critical buckling length.

3.3. Drag and Lift Coefficients

As mentioned before, for the mathematical model it is necessary to evaluate the sectional drag and lift coefficients of the rods as a function of the sectional angle of incidence. For circular rods, the drag coefficient of an equivalent rigid rod is measured as $C_D = 0.95$ which is used as the sectional drag coefficient. For the ribbons, the drag and lift coefficients of an equivalent flat metallic strip were measured for a range of incidence angles. To simplify the model, the average of the drag and lift measurements for $Re = 10000$ and 20000 were fitted using trigonometric functions (see the supplementary file):

$$C_D(\psi) = 1.37 |\cos(\psi)| + 0.05, \quad (36)$$

$$C_L(\psi) = 0.80 \sin(2\psi). \quad (37)$$

The flat metallic strip possessed the same dimensions as the flexible ribbons (400×25.4 mm). Moreover, the measured pitching moment was found to be very small with respect to the torsional rigidity of ribbons therefore it was neglected in the mathematical model.

3.4. Drag of Flexible Specimens

Herein, the wind tunnel results represent the time-averaged values of fluctuating loads measured over 30 seconds. The time-averaged values exhibit a standard deviation of less than 10 percent, or else are deemed unacceptable and are discarded. At high velocities, the rods and the ribbons underwent large amplitude vibrations possibly due to turbulence buffeting, although some flutter or galloping phenomena cannot be ruled out. For the lowest flow velocity in the experiments, the vortex shedding frequency is estimated to 40 Hz for a Strouhal number of 0.2. This frequency is largely beyond the fundamental frequency of the tested ribbons and circular rods which is of the order of 2 Hz [18]. In the results presented here, only the static deformations of the rods and ribbons are considered.

In reality, plants can be subjected to wind loading from any direction. The present work shows that the drag on a specimen is highly dependent on the incidence angle. Figure 3a and Fig. 3b show rose plots of drag force on chiral circular rods at $U = 13 \text{ ms}^{-1}$ and ribbons at $U = 15 \text{ ms}^{-1}$, respectively. On the rose plots, the radial distance of points indicates the drag loading magnitude as a function of the angle of incidence, i.e. the loading direction. In the figures, each curve represents a simulation for a fixed value of the intrinsic twist angle while symbols represent its equivalent experimental data. The aforementioned flow velocities were selected for large deformations with a maximum number of valid wind tunnel tests. A range of 90° for ψ_0 was tested in the wind tunnel. However, depending on the initial alignment and the handedness of chiral specimens, either the range of $\psi_0 = 0^\circ$ to 90° or $\psi_0 = 90^\circ$ to 180° was measured. As seen, the drag force strongly varies with the wind direction for a non-chiral rod and ribbon. As the intrinsic twist angle increases, both plots approach a perfect circle meaning that the drag becomes less direction dependent. It should be noted that some of the experimental data are missing in the plots because they were not acceptable due to a standard deviation larger than 10 percent.

To better understand the effect of chirality, for each intrinsic twist angle, we vary the incidence angle to maximize and minimize drag. Figure 3c and Fig. 3d show the mathematical prediction of these extremums for chiral circular rods and ribbons for a range of the intrinsic twist angle τ_0 from 0° to 720° . In these figures, the relative drag of rigid circular rods as well as the maximum and minimum drag of equivalent rigid ribbons are provided for reference. In the mathematical model, the relative drag of chiral rods and ribbons with a specific chiral angle τ_0 , is evaluated for a range of ψ_0 from 0° to 360° . The maximum and minimum relative drag can be found at any angle in this range

depending on τ_0 . The relative drag force is calculated as $D_r = D/D_0$ where D_0 is the drag of a rod with $\tau_0 = 0^\circ$ and $\psi_0 = 0^\circ$. The markers represent the experimental drag data regardless of the incidence angle. The relative drag force of a non-chiral rod is maximum at $\psi_0 = 90^\circ$ and minimum at $\psi_0 = 0^\circ$. On the other hand, the relative drag force of a non-chiral ribbon is maximum at $\psi_0 \approx 45^\circ$ and the minimum at $\psi_0 = 90^\circ$. The reason is that the projected area of a circular rod does not change with ψ_0 but the projected area of a non-chiral ribbon is minimum at $\psi_0 = 90^\circ$ and maximum at $\psi_0 = 0^\circ$. This is valid only for non-chiral rods and ribbons and it is not necessarily applied to chiral ones. In Fig. 3c, the flow velocity is $U = 13 \text{ ms}^{-1}$ which is equivalent to $C_Y = 10$ where reconfiguration is important. For the mathematical model, the average mechanical properties of the circular rods in Table 1 were used. Moreover, a constant $C_D = 0.95$ was considered. As seen, the maximum relative drag decreases and the minimum relative drag increases. This means that the difference between the maximum and the minimum drag decreases indicating that the drag becomes direction independent for high intrinsic twist angles. This is similar to the static bending results presented in Fig. 2a which shows that the chirality makes the deformation of a rod less dependent on the loading direction. It can also be found in Fig. 3c that chirality is beneficial for circular rods since it decreases the fluid loading. Higher drag forces usually lead to higher stresses therefore chirality should be helpful for plants with circular or semi-circular sections in reducing the probability of structural failure.

Fig. 3d presents the relative drag force on chiral ribbons for $U = 15 \text{ ms}^{-1}$ or $C_Y = 20$. It is seen that the minimum and the maximum relative drag increase up to a value of τ_0 of 90° and 180° , respectively. Beyond 180° , the maximum drag decreases. Similarly to Fig. 3c, the range between the maximum and the minimum drag values decreases with increasing intrinsic twist angle. In addition, the drag of rigid ribbons also becomes less directional and approaches an asymptotic value. Similarly, it was reported in [25] that the drag coefficient of a rigid chiral ribbon approaches a constant value for very high twist angles. The maximum and minimum drag of rigid ribbons exhibit a periodic variation with chirality. This periodic variation is less pronounced for flexible ribbons. The reason is that in general, the drag of flexible ribbons is less than rigid ones therefore the variation amplitude of their maximum and minimum drag is also smaller. Moreover, flexible ribbons deform and become aligned with the flow. This reduces the effect of chirality on their drag.

This trend is not present for circular chiral rods because it is related to the complex aerodynamic loading on chiral ribbons. For a chiral cylinder, the aerodynamic loading is governed by a single

constant drag coefficient regardless of the intrinsic twist angle. In this case, the structural effect of chirality governs the drag scaling. On the other hand, a chiral ribbon is affected by both the structural and the aerodynamic aspects of the chiral morphology. The competition between these two aspects of chirality leads to a more complex response in chiral ribbons.

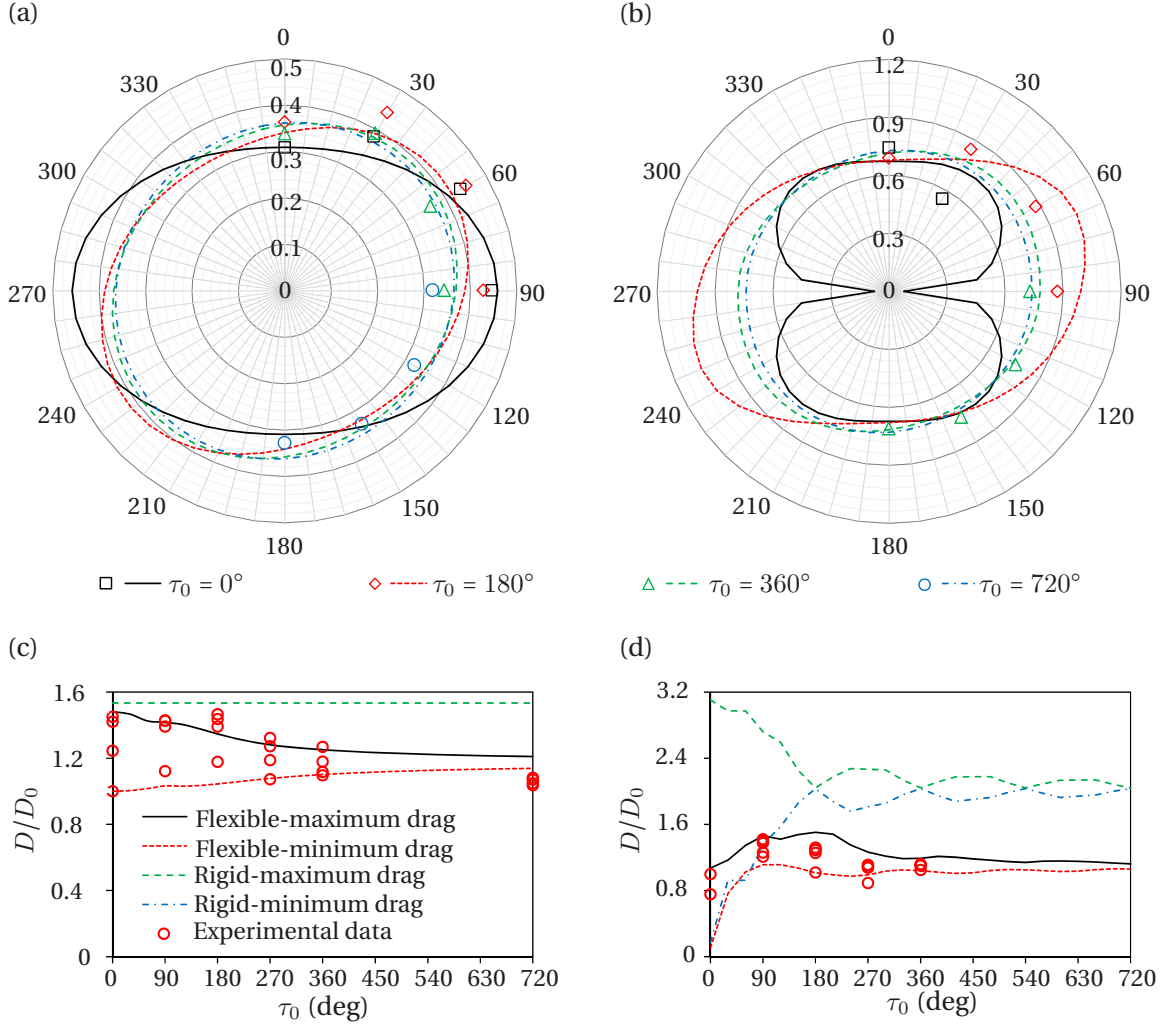


Figure 3: Rose plot of drag as a function of the intrinsic twist angle, τ_0 and the incidence angle, ψ for a) chiral circular rods with $U = 13 \text{ ms}^{-1}$ and b) chiral ribbons with $U = 15 \text{ ms}^{-1}$. c) Maximum and minimum relative drag of chiral circular rods at $U = 13 \text{ ms}^{-1}$ and d) chiral ribbons at $U = 15 \text{ ms}^{-1}$ among a range of incidence angles. Markers represent the experimental data and lines show the mathematical prediction. The maximum and minimum drag of equivalent rigid rods and ribbons are also provided for reference.

3.5. Curvature and Bending Moment

Chirality induces a non-uniform distribution of curvature along the length of the rod or ribbon. This is shown in Fig. 4 for ribbons using the mathematical model. The results are qualitatively

similar for circular rods (not shown). In Fig. 4a, the deformed shape of a non-chiral ribbon with $\psi_0 = 0^\circ$ under a terminal dimensionless bending moment $\bar{M}_Y = M_Y L / (EI)_y = 1.2$ is shown. As expected, the deformation is uniform with a constant curvature. On the other hand, Fig. 4b shows the deformed shape of a chiral ribbon with $\tau_0 = 360^\circ$ under the same loading. As indicated with small arrows, the deformed shape includes three regions of concentrated curvature which we call “nodes”. Moreover, the amplitude of deformation is smaller compared with a non-chiral ribbon because the overall effective bending rigidity is increased due to the twist of the material frame along the centerline. To understand this, the total curvature $\kappa_t = \sqrt{\kappa_x^2 + \kappa_y^2}$ of weightless deforming ribbons under a terminal moment $\bar{M}_Y = 1.2$ with $\psi_0 = 0^\circ$ is presented as a contour plot in Fig. 4e. The contour shows the variation of the total curvature along the ribbon’s length for a range of τ_0 from 0° to 720° . The nodes can be recognized in the contour as the dark regions. For instance, for $\tau_0 = 360^\circ$ we can find three distinctive dark regions in the contour which represent three nodes. As seen, by increasing the intrinsic twist angle, the number of nodes increases. Therefore, we say that chirality “discretizes” the deformation.

Figure 4c shows a non-chiral upright ribbon and Fig. 4d shows a chiral upright ribbon ($\tau_0 = 360^\circ$) both deforming under wind and gravity with $C_Y = 30$ and $\psi_0 = 0^\circ$. Similarly to the previous case, the non-chiral ribbon undergoes a smooth deformation while the deformed chiral ribbon has two distinctive curvature nodes. Moreover, the deformation of the chiral ribbon is smaller because its overall rigidity is higher due to chirality. Fig. 4f shows a contour of the total curvature for upright ribbons in flow with the same aforementioned conditions. Similarly to the case with a terminal moment, it is found that chirality “discretizes” the deformation and the number of nodes increases with chirality. For instance, there are two nodes for $\tau_0 = 360^\circ$ at $\bar{s} = 0$ and 0.4 and four nodes for $\tau_0 = 720^\circ$ at $\bar{s} = 0, 0.25, 0.5$ and 0.75.

An excessive turning moment may uproot a plant. To study the effect of chirality on the maximum root bending moment of chiral plants, we model mathematically five cases as described in Table 2 to cover a variety of structural and flow parameters. It should be noted that a negative value for \mathcal{W} indicates that the specimen is upright and a positive value represents a buoyant one. The structural properties for the flexible ribbons and weightless rods are based on our experimental specimens. The structural properties of eelgrass (*Zostera*) and daffodil stem are taken from [2, 26] and [27], respectively. It should be noted that the effect of the daffodil flower on top of the stem is not modeled here. For the cattail leaf (*Typha angustifoli*), the values are the average of mea-

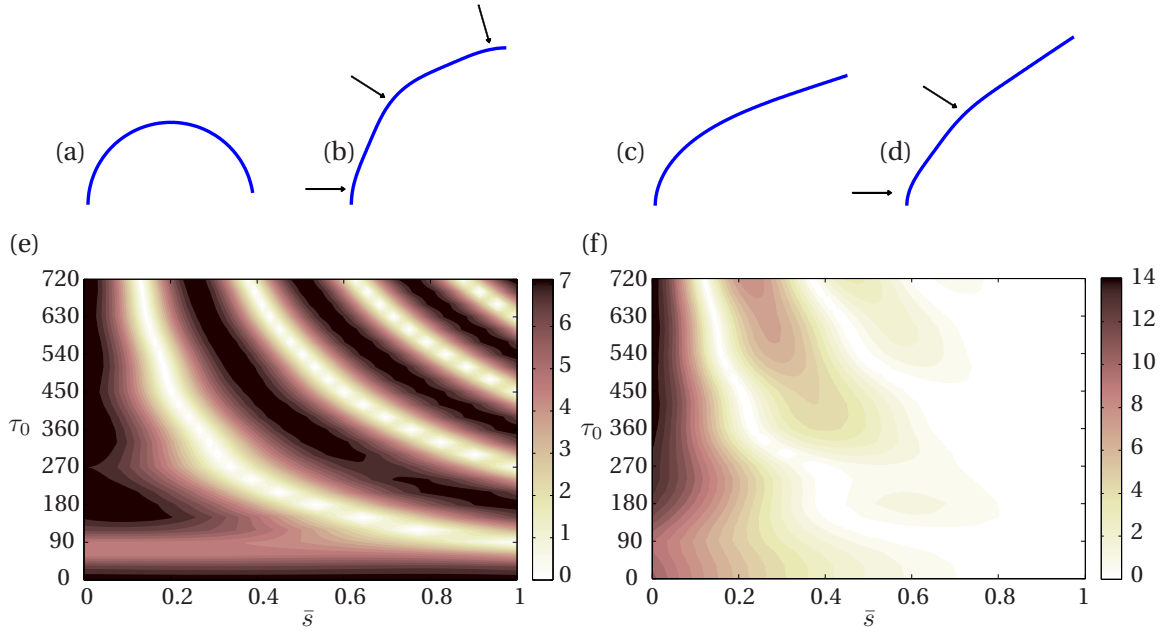


Figure 4: Theoretical evaluation of the deformed shape of weightless ribbons under a terminal moment with a) $\tau_0 = 0^\circ$ and b) $\tau_0 = 360^\circ$. Deformed shape of upright ribbons under the wind loading with c) $\tau_0 = 0^\circ$ and d) $\tau_0 = 360^\circ$. Contour of the total curvature κ_t for e) weightless chiral ribbons under a terminal moment and f) upright ribbons in the flow. The terminal moment is $\bar{M}_Y = 1.2$, the Cauchy number is $C_Y = 30$ and ψ_0 is null for all cases. Small arrows show the curvature nodes on the deformed ribbons.

measurements which we did on several leaves. Twelve mature leaves were collected from the Voyageur Provincial Park (ON, Canada) in August, 2016. Three-points bending tests were done on segments of the leaves to evaluate their bending rigidity, one day after being collected. It was found that the bending rigidity of a cattail leaf decreases significantly from root to tip mainly due to the reduction of its thickness. Therefore, the average of the bending rigidity, width and thickness of multiple leaf segments was used in the mathematical model. Based on present experiments on cattail leaves, the bending rigidity varies from $0.03 \times 10^{-3} \text{ Nm}^2$ for the tip section to $3.9 \times 10^{-3} \text{ Nm}^2$ for the root section. This shows two orders of magnitude of change in the bending rigidity from tip to root. The average bending rigidity for the cattail leaves is $0.87 \times 10^{-3} \text{ Nm}^2$. Moreover, λ varies for the tested cattail leaves from 0.0025 to 0.1 with an average of 0.032 (see the supplementary file for more de-

Table 2: Physical properties of study cases

Case	Section	L (cm)	d (mm)	t (mm)	$(EI)_y$ (Nm ²)	η	λ	\mathcal{W}	C_Y
Flexible Ribbon	Rectangular	40	25.4	1.2	0.01	0.675	0.0022	-1.93	30
Ealgrass	Rectangular	40	8	0.35	$2.8e-5$	1	0.0019	20	30
Cattail leaf	Rectangular	65	7.6	1.26	$0.87e-3$	1	0.032	-6.6	30
Weightless Rod	Circular	26	19	-	0.0033	1.25	0.16	0	30
Daffodil Stem	Semi-circular	27	8.5	-	0.012	13.3	0.5	-0.92	30

tail). Using the model, the maximum value of the dimensionless bending moment \bar{M}_{max} computed over a range of incidence angles from 0° to 180° is plotted for the aforementioned cases in Fig. 5, where $\bar{M} = L\sqrt{\bar{M}_x^2 + \bar{M}_y^2}/(EI)_y$. The plots illustrate the variation of \bar{M}_{max} at root as a function of the intrinsic twist angle τ_0 . For the daffodil stem, an aerodynamic model similar to a circular rod is used although in reality, the cross section is semi-circular or elliptic. Moreover, the bending rigidity ratio λ for the daffodil stem is calculated as the ratio of the second moment of area around the two sectional axes of symmetry (I_y/I_x). As seen, the variation of \bar{M}_{max} is different between the ribbons with rectangular sections and rods with circular or semi-circular sections. For the circular or semi-circular cases, \bar{M}_{max} at root decreases with increasing τ_0 and approaches a constant value for very high intrinsic twist angles. However, for the cases with a ribbon-like structure, \bar{M}_{max} increases up to a certain value of τ_0 between 120° and 150° ; beyond that, it decreases and approaches a constant value. The mathematical model showed that for cattail leaves in air flow, \bar{M}_{max} is not significantly sensitive to the variation of λ and the bending rigidity. Moreover, the peak value of \bar{M}_{max} is found at 150° for all the study cases. At first glance, the figure suggests that an untwisted structure is better for plants to reduce the root bending moment. However, as we understood from Fig. 2b, chirality increases the buckling strength of upright ribbons which reduces the chance of structural failure. Therefore, chirality brings a trade-off for upright plants with increased buckling strength but also higher root bending moment. For instance, cattail leaves are chiral and according to our measurements, their average intrinsic twist angle is $380^\circ \pm 110^\circ$. The shaded area in Fig. 5 represents the distribution of twist angles of the cattail specimens which we have collected. It should be noted that the intrinsic twist angle of plants may vary with environmental parameters.

The results show that eelgrass is subjected to a larger root bending moment with respect to an upright ribbon and a cattail leaf. The reason is that the buoyancy effect decreases the deformation magnitude which leads to a larger drag as suggested by [2]. A larger drag on the plant's body leads to a larger root moment. In comparison, an upright ribbon and a cattail leaf are subjected to a smaller root moment since their weight contributes to the deformation and drag reduction. On the other hand, the reconfiguration of the daffodil stem is highly affected with its large η . This means that the daffodil stem easily reorients to its less rigid direction which leads to a large deformation. The large deformation of the daffodil then reduces the drag and the root moment. However, as seen in Fig. 5, a weightless rod with a smaller η than the daffodil stem, has a larger root bending moment. This is specifically interesting since it is known that many plants twist more easily than they bend [28],

which shows that low torsional rigidity is beneficial for plants to reduce the risk of uprooting.

According to Eq.(1), \bar{M}_{max} is created at the root due to the contribution of the curvatures in the x and y -directions. Although κ_x is usually smaller than κ_y , its contribution to the bending moment is usually more important due to the higher bending rigidity. This means that uprooting happens because of an excessive bending moment created in the stiffer direction of the plant. Finally, the difference in behavior between structures with rectangular sections and those with circular or semi-circular sections comes from the different aerodynamic loadings on these structures.

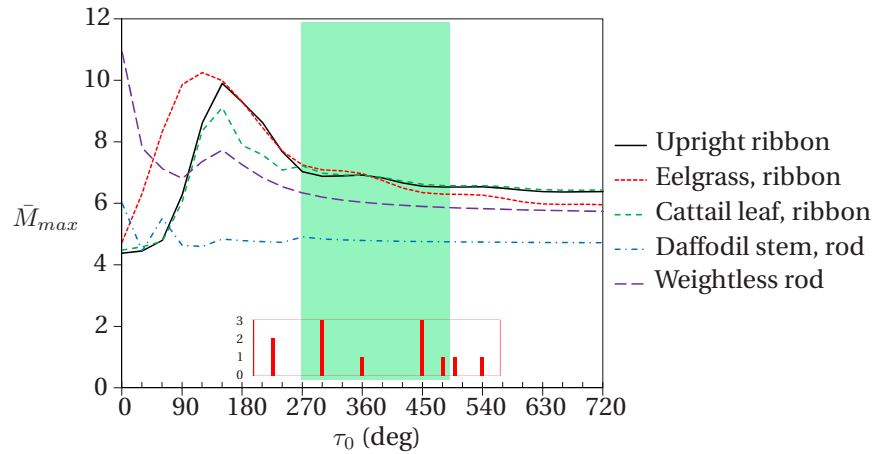


Figure 5: Maximum dimensionless bending moment at root of five study cases at $C_Y = 30$. Plots are predicted using the mathematical model. The shaded area represent the range of the most probable intrinsic twist angle of the cattail specimens collected for this study. The small histogram plot shows the distribution of the collected specimens in terms of the intrinsic twist angle.

4. Concluding Remarks

The reconfiguration and buckling of chiral plants was studied using flexible rods and ribbons with a chiral morphology. Wind tunnel experiments were conducted using circular rods with internal reinforcement as well as chiral ribbons. For the theoretical analysis, a Kirchhoff rod model was coupled with a semi-empirical drag and lift formulation. The theoretical model provides a general framework to study the large deformation of rods and ribbons as well as slender wings in flow. It was shown that chirality increases the critical buckling length and consequently the buckling strength of upright slender structures under their own weight. Chirality was found to render the rods and ribbons less dependent on the direction of external loading such as gravity or wind. Moreover, chiral rods and ribbons show a non-smooth deformation with one or more nodes in their deformed shape due to their geometrical twist. Thus chirality can be said to “discretize” the deformation.

The theoretical model predicts that for circular rods, chirality decreases the root bending moment. On the contrary, the root bending moment of chiral ribbons is higher than a straight ribbon, especially at intermediate angles of chirality around $\tau_0 \approx 150^\circ$. Despite this, many upright plants show a chiral morphology possibly due to its aforementioned benefits including higher buckling strength and weaker dependency on the loading direction. Our measurements on chiral cattail leaves showed that the distribution of their inherent twist angle bypasses the intermediate chiral angles and is centered around a large chiral angle. However, it is of interest to perform measurements on more chiral species which grow upright, to verify their angle of chirality. It is also recommended to account for the variation of the sectional area and bending rigidity along the length in the mathematical model to represent real plant organs such as leaves and stems. Moreover, further experimental and theoretical investigations should be done to study the effect of chirality on the dynamic stability of chiral plants against flutter and vortex-induced vibration.

Acknowledgment

The financial support of the Natural Sciences and Engineering Research Council of Canada is acknowledged.

References

- [1] S. Vogel, Drag and reconfiguration of broad leaves in high winds, *Journal of Experimental Botany* 40 (1989) 8.
- [2] M. Luhar, H. M. Nepf, Flow-induced reconfiguration of buoyant and flexible aquatic vegetation, *Limnology and Oceanography* 56 (2011) 2003–2017.
- [3] S. Alben, M. Shelley, J. Zhang, Drag reduction through self-similar bending of a flexible body, *Nature* 420 (2002) 479–481.
- [4] S. Alben, M. Shelley, J. Zhang, How flexibility induces streamlining in a two-dimensional flow, *Physics of Fluids* 16 (2004) 1694.
- [5] F. P. Gosselin, E. de Langre, B. A. Machado-Almeida, Drag reduction of flexible plates by reconfiguration, *Journal of Fluid Mechanics* 650 (2010) 319.
- [6] F. P. Gosselin, E. de Langre, Drag reduction by reconfiguration of a poroelastic system, *Journal of Fluids and Structures* 27 (2011) 1111–1123.
- [7] L. Schouveiler, A. Boudaoud, The rolling up of sheets in a steady flow, *Journal of Fluid Mechanics* 563 (2006) 71.
- [8] Z.-L. Zhao, H.-P. Zhao, B.-W. Li, B.-D. Nie, X.-Q. Feng, H. Gao, Biomechanical tactics of chiral growth in emergent aquatic macrophytes, *Scientific Reports* 5 (2015) 12610.
- [9] H.-M. Ye, J.-S. Wang, S. Tang, J. Xu, X.-Q. Feng, B.-H. Guo, X.-M. Xie, J.-J. Zhou, L. Li, Q. Wu, G.-Q. Chen, Surface Stress Effects on the Bending Direction and Twisting Chirality of Lamellar Crystals of Chiral Polymer, *Macromolecules* 43 (2010) 5762–5770.
- [10] X. Chen, S. Yang, S. Motojima, M. Ichihara, Morphology and microstructure of twisting nanoribbons prepared using sputter-coated Fe-base alloy catalysts on glass substrates, *Materials Letters* 59 (2005) 854–858.
- [11] Z.-L. Zhao, H.-P. Zhao, J.-S. Wang, Z. Zhang, X.-Q. Feng, Mechanical properties of carbon nanotube ropes with hierarchical helical structures, *Journal of the Mechanics and Physics of Solids* 71 (2014) 64–83.

- [12] K. Schulgasser, A. Witztum, Spiralling upward, *Journal of theoretical biology* 230 (2004) 275–280.
- [13] J. I. Lunine, J. Beauchamp, M. A. Smith, E. Nikolaev, The Abiotic Generation of Homochirality on Saturn's Moon Titan, in: *Advances in BioChirality*, volume 257, 1999.
- [14] U. Rowlatt, H. Morshead, Architecture of the leaf of the greater reed mace, *typha latifolia* L., *Botanical journal of the Linnean Society* 110 (1992) 161–170.
- [15] A. Goriely, P. Shipman, Dynamics of helical strips, *Physical Review E* 61 (2000) 4508.
- [16] J.-S. Wang, H.-M. Ye, Q.-H. Qin, J. Xu, X.-Q. Feng, Anisotropic surface effects on the formation of chiral morphologies of nanomaterials, *Proceedings of the Royal Society A: Mathematical, Physical and Engineering Sciences* 468 (2012) 609–633.
- [17] J.-S. Wang, Y.-H. Cui, T. Shimada, H.-P. Wu, T. Kitamura, Unusual winding of helices under tension, *Applied Physics Letters* 105 (2014) 043702.
- [18] M. Hassani, N. W. Mureithi, F. P. Gosselin, Large coupled bending and torsional deformation of an elastic rod subjected to fluid flow, *Journal of Fluids and Structures* 62 (2016) 367–383.
- [19] E. H. Dill, Kirchhoff's theory of rods, *Archive for History of Exact Sciences* 44 (1992) 1–23.
- [20] B. Audoly, Y. Pomeau, *Elasticity and geometry: from hair curls to the non-linear response of shells*, Oxford University Press Oxford, 2010.
- [21] G. Taylor, Analysis of the swimming of long and narrow animals, *Proceedings of the Royal Society A: Mathematical, Physical and Engineering Sciences* 214 (1952) 158–183.
- [22] S. K. Chakrabarti, *The theory and practice of hydrodynamics and vibration*, volume 20, World scientific, 2002.
- [23] E. de Langre, Effects of wind on plants, *Annual Review of Fluid Mechanics* 40 (2008) 141–168.
- [24] E. Doedel, J. P. Kernevez, *AUTO, software for continuation and bifurcation problems in ordinary differential equations*, California Institute of Technology, 1986.
- [25] B. Cucuel, *Mise en évidence des paramètres influant sur les forces fluides et établissement de modèles empiriques de la traînée de objets à géométrie variable*, Master's thesis, École Polytechnique de Montréal, 2016.

- [26] M. A. Abdelrhman, Modeling coupling between eelgrass *Zostera marina* and water flow, *Marine Ecology Progress Series* 338 (2007) 81–96.
- [27] S. Etnier, S. Vogel, Reorientation of daffodil (*narcissus*: Amaryllidaceae) flowers inwind: drag reduction andtorsional flexibility, *American Journal of Botany* 87 (2000) 29–32.
- [28] S. Vogel, Twist-to-bend ratios and cross-sectional shapes of petioles and stems, *Journal of Experimental Botany* 43 (1992) 1527–1532.